Available online at www.sciencedirect.com

jmr&t Journal of Materials Research and Technology

www.jmrt.com.br

Original Article

New photocatalytic materials obtained from the recycling of alkaline and Zn/C spent batteries

Lorena Alcaraz[a], Irene García-Díaz[a], Laura González[b], María Eugenia Rabanal[c], Ana Urbieta[d], Paloma Fernández[d], Félix A. López[a,*]

[a] Centro Nacional de Investigaciones Metalúrgicas (CENIM-CSIC), Avda. Gregorio del Amo 8, E-28040 Madrid, Spain
[b] IMDEA-Nanociencia, Campus Universitario de Cantoblanco, Madrid 28049, Spain
[c] Universidad Carlos III de Madrid & IAAB, Dpto. de Ciencia e Ingeniería Química, Avda. de la Universidad 30, 28911 Leganés, Madrid, Spain
[d] Universidad Complutense de Madrid, Dpto. de Física de Materiales, Facultad de Ciencias Físicas, Ciudad Universitaria s/n, 28040 Madrid, Spain

ARTICLE INFO

Article history:
Received 16 January 2019
Accepted 22 April 2019
Available online 18 May 2019

Keywords:
Spent batteries
Photocatalytic materials
Zn and Mn oxides
Methylene blue
Rhodamine B

ABSTRACT

Several phases with variable stoichiometry $Zn_xMn_{3-x}O_4$ (with x = 0.25, 0.85 and 1) and ZnO have been obtained from the black mass, a widely generated residue of wasted alkaline batteries. The obtained samples have been characterized by X-ray diffraction (XRD) and Raman spectroscopy showing results consistent with the stoichiometry obtained from chemical analysis. The study of the degradation of methylene blue (MB) and rhodamine B (RhB) under UV radiation demonstrates the photocatalytic behavior in all samples obtained, reaching degradation percentages higher than 70% and 50%, respectively.

1. Introduction

The great development and continuous growth of the population have contributed to a considerable increase in global environmental pollution. For example, industries dump to wastewater between 300 and 400 million tons each year of different pollutants such as heavy metals, solvent and toxic sludge [1]. These residues cause significant environmental problems, so their elimination is of particular importance due to its potentially harmful effect [2].

The legal regulations impose ever stricter criteria to validate the quality of residual waters (maximum values of contaminant to be considered clean or decontaminated), hence the growing interest generated in the search for new methods for the efficient elimination of pollutants [3].

Traditionally the technologies used for cleaning water are mainly based on adsorption processes using activated carbon, or desorption in the air [4], however, these processes only transfer the pollutants from the aqueous solution to another phase, still contaminated, then the problem persists. This scenario has pushed the development of new technologies based on photocatalytic oxidation and consequently, the search for chemicals with a high oxidation power that could lead to an efficient degradation of the pollutants. In these processes, the

* Corresponding author.
E-mail: f.lopez@csic.es (F.A. López).
https://doi.org/10.1016/j.jmrt.2019.04.020

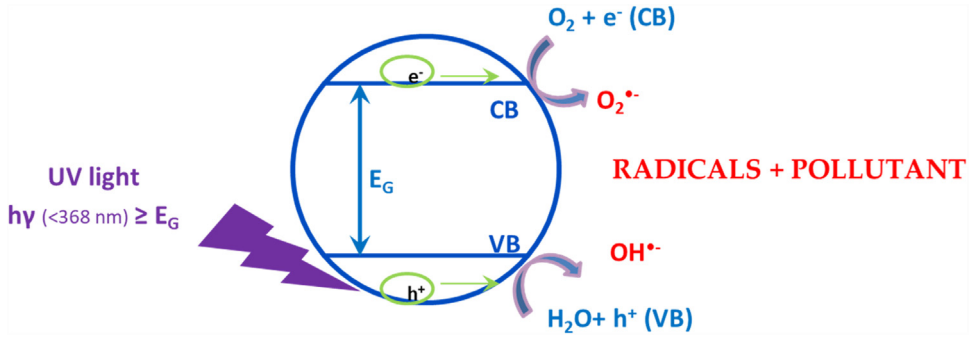

Fig. 1 – Scheme of the photocatalytic process.

radicals generated in the oxidation, react with the pollutant, rendering products environmentally harmless [4]. The variety of contaminants that can be eliminated from water by catalytic oxidation assisted by solar radiation goes from organic substances like dyes or pesticides [5–7] to heavy metals [1,3].

The photocatalytic reaction is initiated when a photoexcited electron of a photocatalyst semiconductor is promoted from the valence band filled with a semiconductor photocatalyst to the empty conduction band being the energy of the absorbed photons ($h\nu$) is equal to or greater than the energy of the band gap of the photocatalyst [8]. The absorption of photons causes the excitation and transfer of electrons (e^-) from the valence band (VB) to the conduction band (e^-_{CB}), leading to the generation of holes (h^+) in the valence band (h^+_{VB}). Next, the migration of the charge carriers (e^- and h^+) to the surface of the photocatalyst occurs. Highly reactive electrons and holes tend to carry out reduction and oxidation reactions to produce hydroxyl radicals ($^\bullet OH$) and superoxide anion radicals ($O_2^{\bullet-}$), respectively, which subsequently react by degrading the contaminant [2], as shown in the scheme of Fig. 1.

Different semiconductor materials, in particular oxides, have been used such as titanium dioxide (TiO_2), zinc oxide (ZnO), tungsten oxide (WO_3) or hematite (α-Fe_2O_3), proving to be effective photocatalyst [5]. Most of these semiconductors have wide band gaps (above 3.2 eV), showing photocatalytic activity after illumination with UV radiation [7]. However, this bandwidth limits its response under direct sunlight, that would be desirable, since the UV fraction is only around 3–5% of the whole spectrum. Another limiting factor is the rapid recombination of photogenerated electron-hole pairs (e^-–h^+), the catalytic photodegradation requires the generation of reactive oxygen species (ROS) such as hydroxyl ($^\bullet OH$) or superoxide ($O_2^{\bullet-}$) radicals and H_2O_2, that cannot occur if the e^-–h^+ recombination is too fast [6]. Different routes such as semiconductor coupling [9] or doping [10] are currently being studied in order to overcome these limitations and improve the photoresponse of these materials.

Doping the semiconductor materials with metals, in particular transition metals (TM), increases the number of surface defects [11] and therefore affects the optical and electronic properties [12]. The incorporation of a TM in the oxide does not, in principle modify its band gap, but introduces defect levels in the mid-gap that enable transitions at energies below the band gap, then extending the usable fraction of solar spectrum [2,13,14].

In the present work, the photocatalytic activity of Zn and binary Zn/Mn oxides obtained from the black mass of spent alkaline batteries has been studied. The recovery process has been described elsewhere [14–16]. Doping with manganese is very promising due to different oxidation states are possible for this ion (Mn^{2+}, Mn^{3+} and Mn^{4+}) and the consequent ability to act as electron or hole trap [17–19].

2. Materials and methods

2.1. *Sample preparation*

2.1.1. *Obtaining of phases of stoichiometry $Zn_xMn_{3-x}O_4$ (with x = 0.25, 0.85 and 1)*

The black starting mass for obtaining the different binary oxides was provided by Envirobat España, S.A. (Guadalajara, Spain). This black mass comes from the dismantling of alkaline and Zn–C batteries.

To obtain the different oxides, 100, 200 or 300 g of black mass were dissolved in 1 L of a solution of: milliQ water (500 mL), 7.5 M HCl (250 mL) and 0.7 M H_2O_2 (250 mL). The mixtures were homogenized and, after 1 h at room temperature (RT), were filtered using a Millipore Holder filter at 7 bar pressure. The liquids collected (pH ~ 0) were treated adding 6 M NaOH until reaching a pH value between 12 and 14, and the solids obtained were discarded. Finally, the mixtures are filtered obtaining the corresponding binary oxides of stoichiometries $Zn_xMn_{3-x}O_4$ (with x = 0.25, 0.85 and 1) for the solid/liquid ratios of 100, 200 and 300 g/L, respectively.

2.1.2. *Obtaining of the phases of stoichiometry ZnO*

ZnO samples were obtained by two different routes: precipitation (ZnOp) and thermal decomposition (ZnOc). In the first case, after the alkaline precipitation described above, HCl is added to the collected liquids, until pH decreases from the initial value (12–14) to a value of 9.5. From this step, a white precipitate (ZnOp), that will be separated by filtration and subsequently dried, is obtained. In the second route (ZnOc), the precursor $Zn_5(CO_3)_2(OH)_6$ obtained after the leaching of the

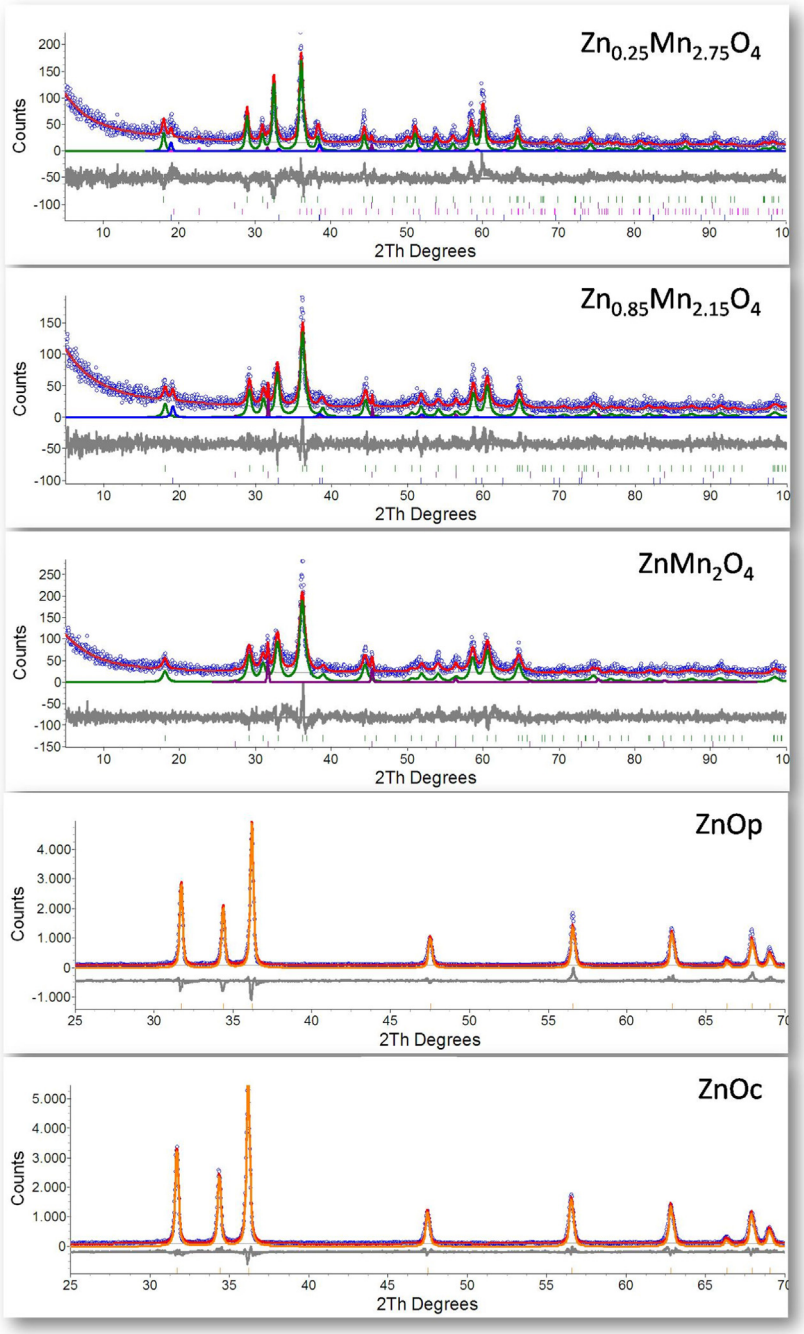

Fig. 2 – Experimental and Rietveld-refined XRD patterns of $Zn_xMn_{3-x}O_4$ and ZnO samples.

black mass with a solution of $(NH_4)_2CO_3/NH_3$ is calcined at 800 °C for 5 h under constant air flow [14].

2.2. *Characterization*

The structural characterization was carried out by means of X-ray diffraction (XRD) using a Siemens D5000 diffractometer equipped with a Cu anode (Cu Kα radiation) and a LiF monochromator. Rietveld method was applied for the calculation of structural parameters from XRD patterns. We have used the version 4.2 of the Rietveld analysis program TOPAS (Bruker ASX) and crystallographic information of the different phases obtained from Pearson's crystal structure database for inorganic compounds release [20].

Micro-Raman spectra were obtained using a confocal Horiba Jovin-Ybon Lab RAM HR800 system. The samples were excited by a 633 nm He–Ne laser on an Olympus BX 41 confocal microscope with a 10× objective. A charge coupled device detector was used to collect the scattered light dispersed by 600 lines mm^{-1} grating (micro-Raman). The spectral resolution of the system used was 1.5 cm^{-1} for the measurements.

All samples were characterized by UV–visible diffuse reflectance spectra (DRS) measuring in the range of 350–500 nm and 450–650 for methylene blue (MB) and rhodamine B (RhB) at RT using a UV–visible Spectrophotometer (Varian Cary 100 with DRA-CA-30I Diffuse Reflectance Accessory).

The photocatalysis experiments were carried out in a Pyrex glass reactor at RT. 5 mg of solid catalyst was dispersed in 600 mL of MB and RhB solutions of concentration 2.5 mg/L, and the mixture was magnetically stirred during 20 min without illumination, to obtain a homogeneous suspension and reach the adsorption equilibrium. The photocatalytic degradation was carried out for until equilibrium is reached, in continuous stirring under UV-light irradiation (365 nm), in a dark room with 125 W high-pressure mercury vapor lamp (Jinfei Company, Shanghai). Aliquots (3 mL) of the solution extracted every 10 min (every 15 min for times larger than 75 min) are studied by UV–Vis absorption in a Lambda 14P UV–visible Spectrophotometer to monitor the degradation of both methylene blue and rhodamine B solutions.

3. Results and discussion

3.1. *Ray diffraction*

The structure and phase distribution of the obtained samples were determined by XRD. Fig. 2 shows the analysis of X-ray diffraction patterns after application of the Rietveld method for the samples investigated.

In the case of mixed binary oxides (Zn/Mn) the majority of the more intense reflexions observed can be indexed based on a tetragonal symmetry of space group $I4_1amd$ compatible with a spinel type structure of Zn and Mn, and with the stoichiometry indicated in each plot. In all cases purities of approximately 95% were obtained in all samples.

In the case of pure zinc oxide samples, the diffraction patterns show reflections that can be indexed to a hexagonal symmetry of a $P6_3mc$ space group with a wurtzite structure.

From the X-ray patterns, the average crystallite size (ϕ) was estimated using the Scherrer equation [21] (Eq. (1)):

$$\phi = \frac{0.89\lambda}{\beta \cos\theta} \quad (1)$$

where ϕ is the average crystallite size, 0.89 is the shape factor assuming spherical particles, λ is the X-ray wavelength, β is the full-width at half-maximum (FWHM) of the experimental diffractions and θ is the Bragg's angle.

The calculated average size for the $Zn_xMn_{3-x}O_4$ samples were 55, 43 and 38 nm for $x = 0.25$, 0.85 and 1, respectively, as well as 72 and 85 nm for the ZnOp and ZnOc samples. In binary oxides the size decreases with the increase in the Zn content in the stoichiometry of the samples obtained according to previous studies carried out in similar phases [22]. In the case of the ZnO phases, the ZnOc sample has a larger particle size compared to ZnOp, what is expected due to the preparation method followed to synthesize [23].

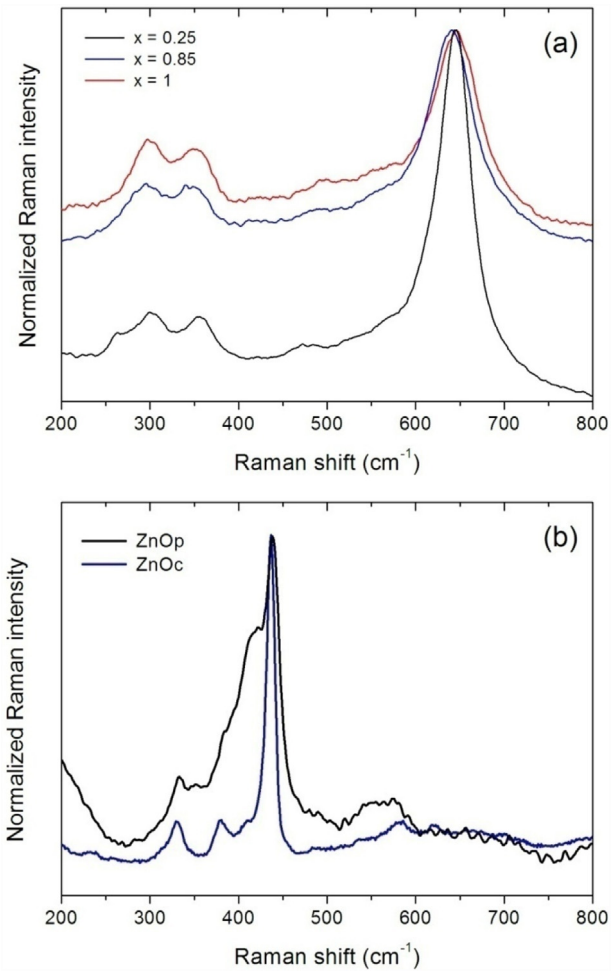

Fig. 3 – Normalized Raman spectra obtained from the samples with the different stoichiometries: (a) $Zn_xMn_{3-x}O_4$ and (b) ZnO.

3.2. *Raman spectroscopy*

Fig. 3 shows the normalized Raman spectra recorded for the different samples obtained. The oxides of stoichiometry $Zn_xMn_{3-x}O_4$ with spinel-like crystalline structure and spatial group $I4_1/amd$ could present, according to group theory, 10 Raman active modes in Raman: $\Gamma = 2A_{1g} + 3B_{1g} + B_{2g} + 4E_g$ [24], however only a few of them are usually observed. The vibration modes with frequencies above 600 cm^{-1} correspond to the movement of the oxygen atoms in the tetrahedral groups AO_4 while the low frequency modes are characteristic of the octahedral sites (BO_6) [24].

In our case, all spectra corresponding to the binary oxides present a maximum around 670 cm^{-1}, typical of the symmetry A_{1g} related to the movement of oxygen (bonding and repulsion effect) of the tetrahedral AO_4 groups [25,26]. It can be seen how, as the manganese content increases, the maxima move toward lower values of Raman shift. In addition, as the Mn content decreases a progressive broadening of the Raman bands is observed showing a loss of crystallinity in the samples (Fig. 3a).

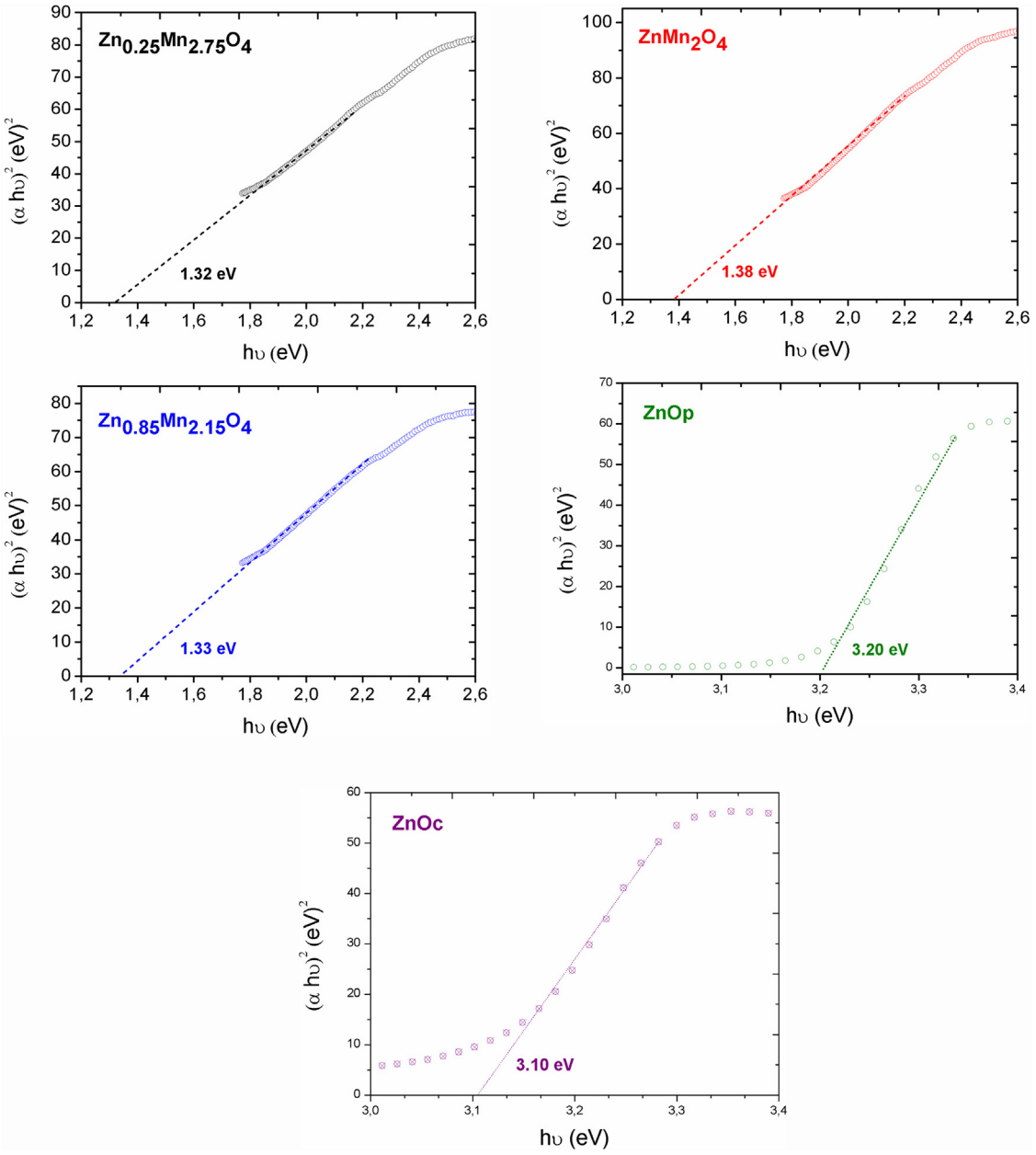

Fig. 4 – Tauc's plots obtained from diffuse reflectance spectra. Absorption coefficients have been obtained by Kubelka–Munk approach.

Regarding non-doped ZnO samples, a wurtzite structure, space group C^4_{6v} with two unit formulas per primitive cell is observed, where all the atoms occupy the C_{3v} sites. In this case, we have four Raman active modes ($A_1 + E_1 + 2E_2$) are possible. A_1 and E_1 modes are polar phonons, and therefore have different frequencies for the transverse optical (TO) and longitudinal optical (LO) modes of vibration because the LO phonons are associated with the macroscopic electric field. On the other hand, the non-polar modes with E_2 symmetry have two different vibration frequencies, associated with the oxygen atoms (E_{2high}) and the Zn sublattice (E_{2low}) [22,27]. These modes are observed at frequencies of 437 cm^{-1} for E_{2high}; 379 cm^{-1} and 410 cm^{-1} for A_1 (TO) and E_1 (TO) respectively; and 541 cm^{-1}, 577 cm^{-1} and 592 cm^{-1} for A_1 (LA), A_1 (LO) and E_1 (LO) respectively [22,28,29].

In the present work, the maxima of the corresponding Raman bands (Fig. 3b) appear close to the reported values, although not all the active modes are observed. As shown in Fig. 3b, the Raman peaks appear at 438 cm^{-1} (E_{2high}), 380 and 411 cm^{-1} (A_1 (TO) and E_1 (TO) respectively). Additional peak at 331 cm^{-1} attributable to E_2(high)-E_2(low) mode is also observed [30]. These results are in agreement with previous studies performed in samples of ZnO obtained by ceramic method and also with those found for thin films [29,30]. On the other hand, the peak broadening observed in ZnOp respect to ZnOc is consequent with lower crystallinity degree observed from the XRD patterns.

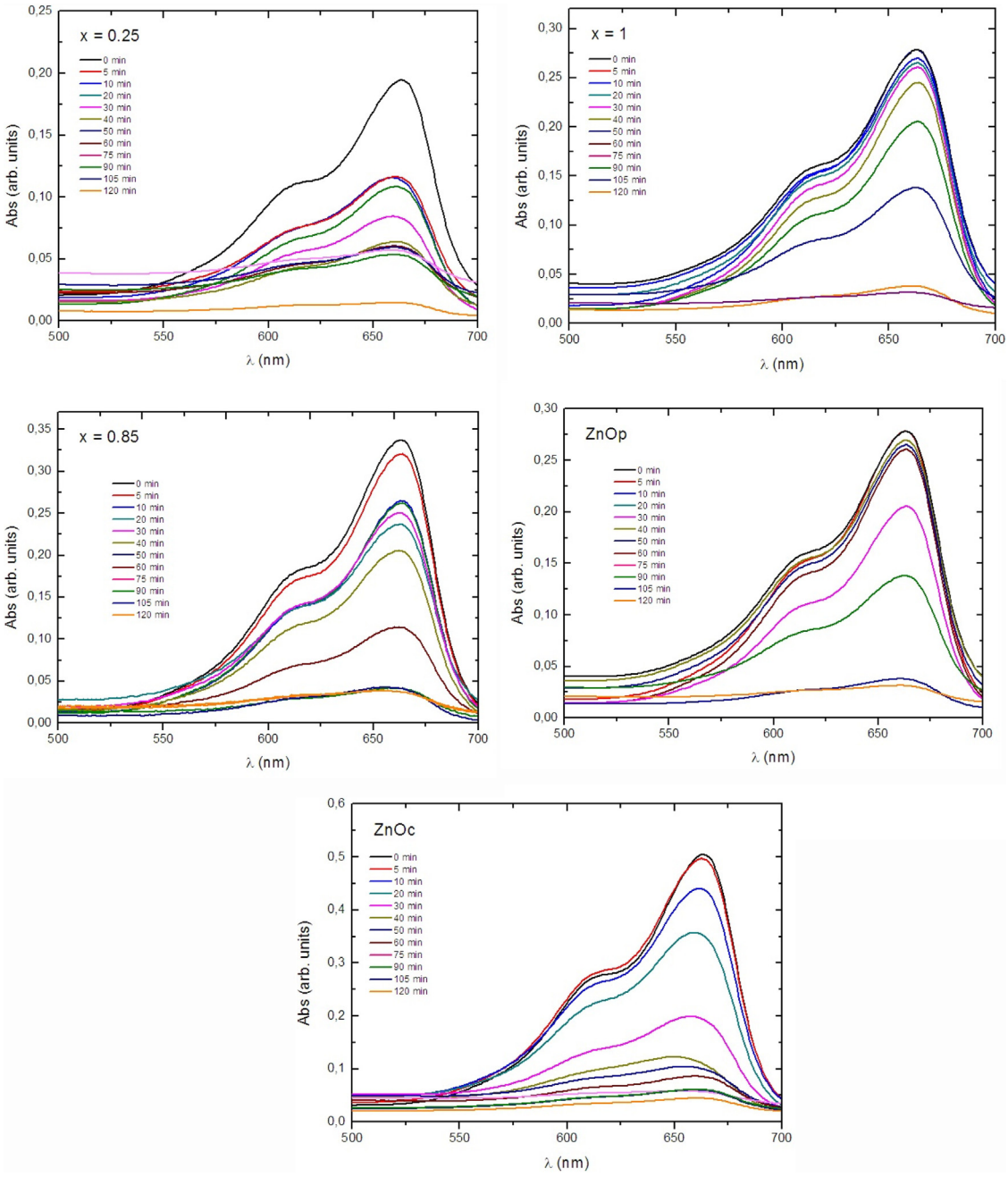

Fig. 5 – Absorption spectra obtained at different illumination times for MB.

3.3. *Optical band gap measurements*

Optical band gap has been obtained from UV–Vis absorption experiments in DRS mode. In order to obtain the energy of the band gap for each of the samples, the Kubelka–Munk and Tauc approaches were used [31,32].

The Kubelka–Munk equation (Eq. (2)) is first used to obtain absorption data from the diffuse reflectance spectrum:

$$F(R_\infty) = \frac{(1 - R_\infty)^2}{2R_\infty} \quad (2)$$

where the term R_∞ represents the reflectance of an infinite film and the function $F(R_\infty)$ is equivalent to the absorption coefficient, α. Then the Tauc plot can be carried out to represent $(\alpha h\nu)^2$ versus $h\nu$, and obtain the optical band gap (E_{gap}) by extrapolation of the linear part of this curve, as shown in Fig. 4. The estimated band gap values obtained decrease when the Mn content increase. The values are similar to those previously reported by other authors in the bibliography, both for the ZnO [33–35], and for Mn doped ZnO samples [36–38].

3.4. *Photocatalysis*

The photocatalytic activity of the samples obtained (both the binary oxides and the zinc oxides) were realized using a UV light lamp and MB and RhB solutions to mimic the

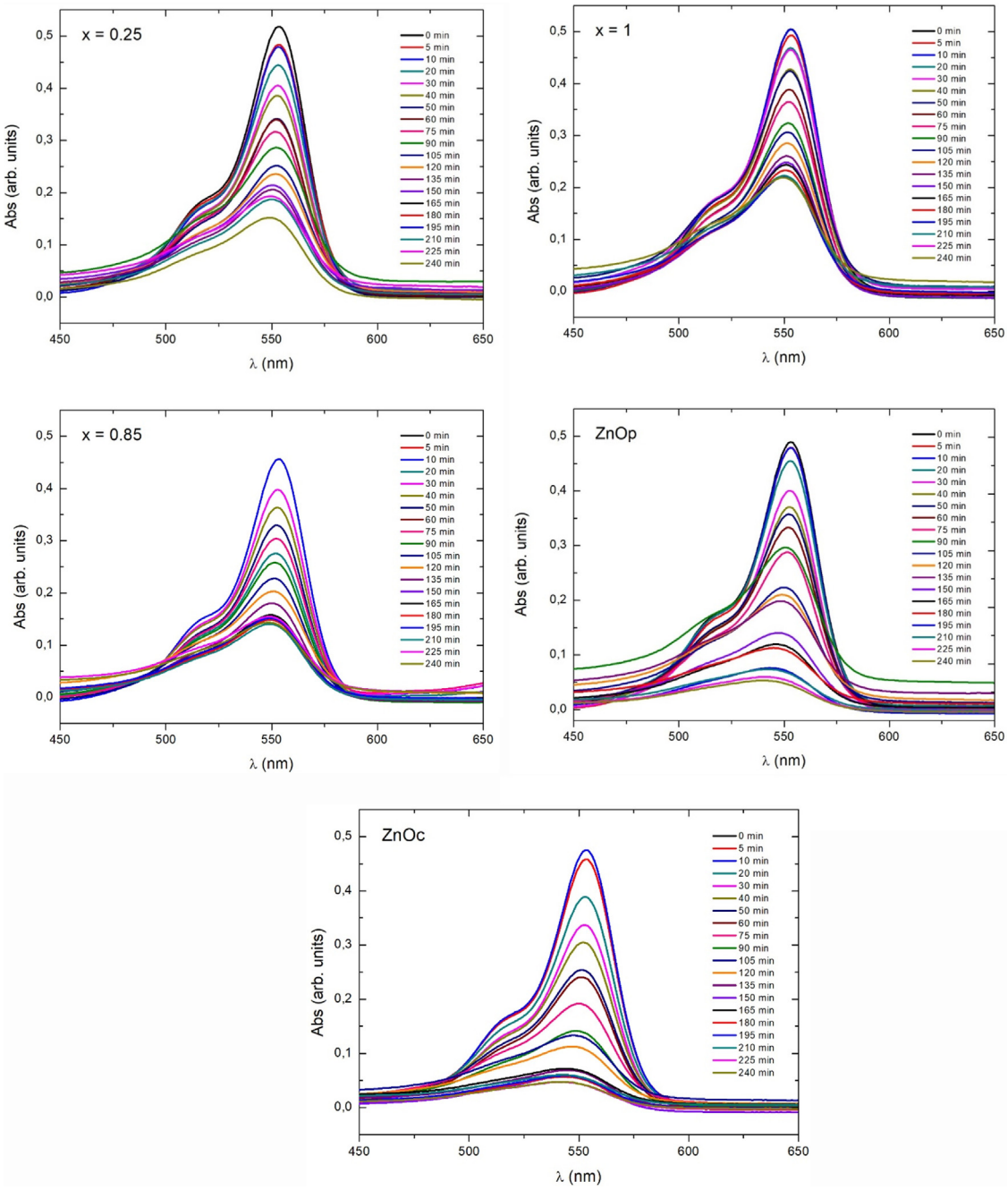

Fig. 6 – Absorption spectra obtained at different illumination times for RhB.

pollutants [39]. To monitor the dye degradation, absorption spectra of aliquot fractions of the solutions are recorded every 10–15 min, and the degradation fraction (δ) and the apparent reaction constants (k) were estimated, according to equations:

$$\delta(\%) = 100\frac{C_0 - C}{C_0} \quad (3)$$

$$k = \frac{1}{t}\ln\frac{C_0}{C} \quad (4)$$

where C_0 is the initial MB or RhB solution concentration and C is the MB or RhB solution concentration at the time (t).

The optical absorbance spectra of all samples are presented in Figs. 5 and 6. Two absorption maxima are observed in both cases, centered around 610 and 660 nm and 510 and 550 nm, characteristic of the absorption spectra of methylene blue [40] and rhodamine B [41]. It can be seen how an increase in the photodegradation reaction time leads to a decrease in absorption bands. As

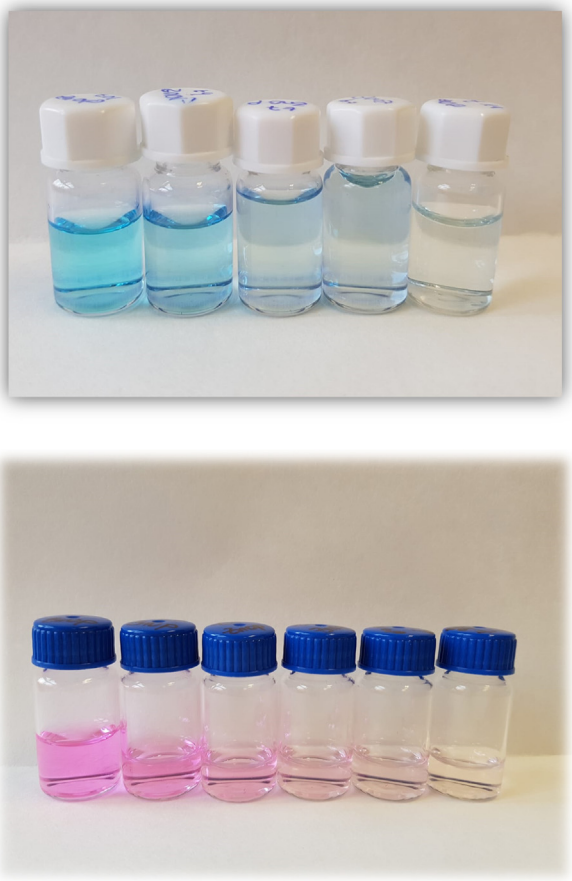

Fig. 7 – Pictures of the corresponding MB and RhB solution of ZnOp sample.

an example, Fig. 7 shows the pictures of the ZnOp sample remaining solution of MB and RhB every 30 min and 60 min, respectively, until reaching the photocatalytic equilibrium.

The study of the kinetics of both pollutants degradation under UV excitation with the different materials was carried out using the pseudo-zero-order linear models (Eq. (5)), pseudo-first-order (Eq. (6)) and pseudo-second-order (Eq. (7)) [42]. Table 1 summarized the obtained results.

$$\text{pseudo-zero-order} [C]_t = [C]_0 - k_{obs,0} \cdot t \quad (5)$$

$$\text{pseudo-first-order} \quad \ln \frac{[C]_t}{[C]_0} = k_{obs,1} \cdot t \quad (6)$$

$$\text{pseudo-second-order} \quad \frac{1}{[C]_t} = \frac{1}{[C]_0} + k_{obs,2} \cdot t \quad (7)$$

where $[C]_t$ is the concentration of MB or RhB at the time t; $[C]_0$ is initial MB or RhB solution concentration and $k_{obs,0}$, $k_{obs,1}$ and $k_{obs,2}$ are the kinetics constants to the pseudo-zero, pseudo-first and pseudo-second order, respectively.

The correlation coefficients R^2 show that reaction kinetics fit better to the pseudo-second-order model. With this model, the experimental kinetic constant can be obtained from the slope of the straight line when $1/[C]_t$ is plotted against the reaction time. The results summarized in Table 1 show that k_{obs} increases with the Zn content, which indicates that the degradation occurs more easily.

Fig. 8 shows the degradation rate of MB and RhB. The maximum degradation is obtained after 60 and 195 min of illumination for MB and RhB, respectively. Thereafter, the degradation percentage remains practically constant. The photocatalytic degradation of RhB is lower than MB similarly to previously reported by others authors to TiO_2 [43] and ZnO [44] samples. Also, the percentage of degradation increases with the increase in the Zn content of the samples (see Table 2). Previous studies carried out on samples of ZnO doped with Mn [2] have shown an increase in photocatalytic activity with the decrease in particle size, agglomeration and the increase in the surface area of the photocatalyst. The results obtained are in good agreement with these studies [2], where the samples with a smaller average size of the crystalline domain obtained from the XRD data present a higher percentage of degradation.

Table 1 – Kinetics constants and correlation coefficients from the different models used for both MB and RhB.

Model	MB degradation									
	x = 0.25		x = 0.85		x = 1		ZnOp		ZnOc	
	k_{obs}	R^2	k_{obs}	R^2	k_{obs}	R^2	k_{obs}	R^2	k_{obs}	R^2
Pseudo-zero-order		0.864		0.874		0.895		0.728		0.693
Pseudo-first-order	0.015	0.932	0.018	0.899	0.019	0.980	0.032	0.977	0.029	0.910
Pseudo-second-order	0.017	0.971	0.238	0.965	0.253	0.987	0.280	0.991	0.391	0.933
Model	RhB degradation									
	x = 0.25		x = 0.85		x = 1		ZnOp		ZnOc	
Pseudo-zero-order		0.899		0.849		0.923		0.936		0.550
Pseudo-first-order	0.064	0.959	0.005	0.916	0.004	0.957	0.009	0.937	0.011	0.951
Pseudo-second-order	0.014	0.992	0.017	0.966	0.019	0.993	0.025	0.966	0.090	0.975

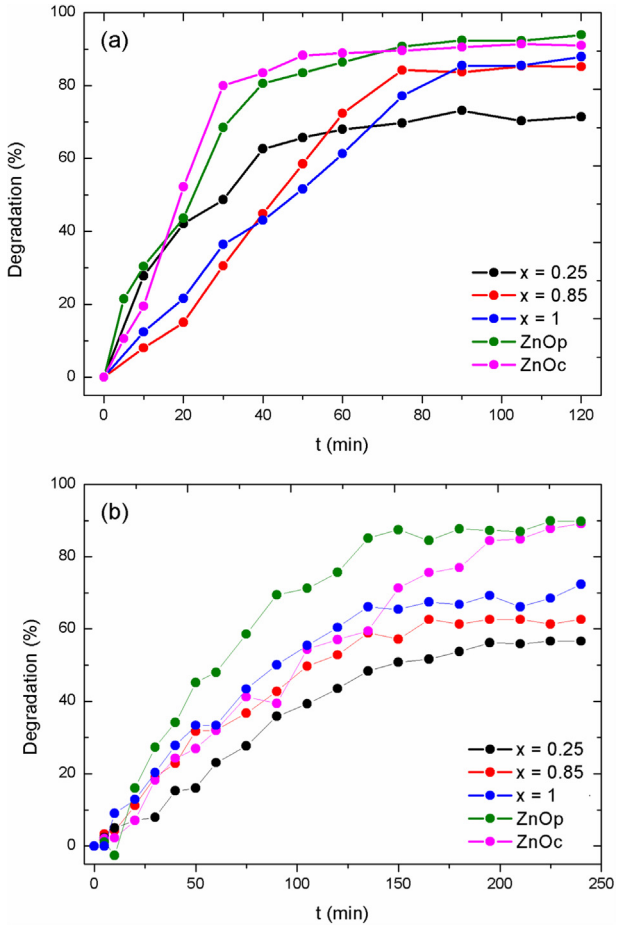

Fig. 8 – Degradation percentage versus photocatalytic reaction time of (a) MB and (b) RhB.

Table 2 – Degradation percentage and E_{gap} values obtained to the different analyzed samples.

Stoichiometry	% MB degradation[a]	% RhB degradation[b]	E_{gap} (eV)
x = 0.25	72	56	1.32
x = 0.85	87	62	1.33
x = 1	89	70	1.38
ZnOp	93	90	3.20
ZnOc	90	89	3.10

[a] Degradation percentage at 120 min reaction time.
[b] Degradation percentage at 240 min reaction time.

4. Conclusions

From the residue obtained of wasted batteries, Mn doped ZnO and ZnO phases have been obtained. The characterization carried out by XRD and Raman spectroscopy show phases consistent with stoichiometries $Zn_xMn_{3-x}O_4$ (with x = 0.25, 0.85 and 1) and ZnO for the samples. In all cases, the samples show a photocatalytic behavior due to the decrease in MB and RhB absorbance in the recorded spectra. The kinetics of the photodegradation reaction are fitted to a pseudo-second-order model. The percentages of degradation for MB and RhB are greater than 70% and 50%, respectively, increasing with the decrease in particle size which leads to an increase in the surface area of the photocatalyst. The band gap values obtained for the analyzed samples are in the range of 1.32–1.38 eV for the samples $Zn_xMn_{3-x}O_4$ and between 3.10 and 3.20 eV for the ZnO samples. In the Mn doped samples, these values increase as the Zn content of the samples increases. The study of the degradation of both MB and RhB under UV radiation was carried out, showing a photocatalytic activity for the possible degradation of pollutants under UV radiation in all the samples investigated.

Conflicts of interest

The authors declare no conflicts of interest.

REFERENCES

[1] Rubio DIC, Calderón RAM, Gualtero AP, Acosta DR, Rojas IJS. Tratamientos para la Remoción de Metales Pesados Comúnmente Presentes en Aguas Residuales Industriales Una Revisión. Rev Ing Y Reg 2015;13:73–90.
[2] Samadi M, Zirak M, Naseri A, Khorashadizade E, Moshfegh AZ. Recent progress on doped ZnO nanostructures for visible-light photocatalysis. Thin Solid Films 2016;605:2–19, http://dx.doi.org/10.1016/j.tsf.2015.12.064.
[3] Fernando L, Giraldo G, Alejandro E, Franco M, Julián J, Arango S. La fotocatálisis como alternativa para el tratamiento de aguas residuales. Rev Lasallista Invest 2003;1:83–92.
[4] Pavas E. Fotocatálisis: una alternativa viable para la eliminación de compuestos orgánicos. Rev Univ EAFIT 2002;Número 127:59–64.
[5] Bhatkhande DS, Pangarkar VG, Beenackers AA. Photocatalytic degradation for environmental applications – a review. J Chem Technol Biotechnol 2002;77:102–16, http://dx.doi.org/10.1002/jctb.532.
[6] Achouri F, Corbel S, Balan L, Mozet K, Girot E, Medjahdi G, et al. Porous Mn-doped ZnO nanoparticles for enhanced solar and visible light photocatalysis. Mater Des 2016;101:309–16, http://dx.doi.org/10.1016/j.matdes.2016.04.015.
[7] Ullah R, Dutta J. Photocatalytic degradation of organic dyes with manganese-doped ZnO nanoparticles. J Hazard Mater 2008;156:194–200, http://dx.doi.org/10.1016/j.jhazmat.2007.12.033.
[8] Abdollahi1 Y, Abdullah1,2 AH, Zainal1 Z. 2 NAY synthesis and characterization of manganese doped ferroxane nanoparticles. Int J Basic Appl Sci 2011;11:44–50, http://dx.doi.org/10.1557/PROC-800-AA9.4.
[9] Wang F, Liang L, Shi L, Liu M, Sun J. CO_2-assisted synthesis of mesoporous carbon/C-doped ZnO composites for enhanced photocatalytic performance under visible light. Dalt Trans 2014;43:16441–9, http://dx.doi.org/10.1039/C4DT02098G.
[10] Erwin SC, Zu L, Haftel MI, Efros AL, Kennedy TA, Norris DJ. Doping semiconductor nanocrystals. Nature 2005;436:91–4, http://dx.doi.org/10.1038/nature03832.
[11] Qi B, Hu Y, Liu H, Dong Z. Photocatalytic degradation and toxic effects of Ag-doped ZnO nanocrystallites. J Nanosci Nanotechnol 2011;11:9513–8, http://dx.doi.org/10.1166/jnn.2011.5281.
[12] Vanheusden K, Warren WL, Voigt JA, Seager CH, Tallant DR. Impact of Pb doping on the optical and electronic properties of ZnO powders. Appl Phys Lett 1995;67:1280–2, http://dx.doi.org/10.1063/1.114397.

[13] Rehman S, Ullah R, Butt AM, Gohar ND. Strategies of making TiO_2 and ZnO visible light active. J Hazard Mater 2009;170:560–9, http://dx.doi.org/10.1016/j.jhazmat.2009.05.064.
[14] López FA, Cebriano T, García-Díaz I, Fernández P, Rodríguez O, Fernández AL. Synthesis and microstructural properties of zinc oxide nanoparticles prepared by selective leaching of zinc from spent alkaline batteries using ammoniacal ammonium carbonate. J Clean Prod 2017;148:795–803, http://dx.doi.org/10.1016/j.jclepro.2017.02.031.
[15] Cebriano T, García-Díaz I, Fernández AL, Fernández P, López FA. Synthesis and characterization of ZnO micro- and nanostructures grown from recovered ZnO from spent alkaline batteries. J Environ Chem Eng 2017;5:2903–11, http://dx.doi.org/10.1016/j.jece.2017.05.052.
[16] Buzatu T, Popescu G, Birloaga I, Săceanu S. Study concerning the recovery of zinc and manganese from spent batteries by hydrometallurgical processes. Waste Manage 2013;33:699–705, http://dx.doi.org/10.1016/j.wasman.2012.10.005.
[17] Kernazhitsky L, Shymanovska V, Naumov V, Fedorenko L, Kshnyakin V, Shcherban N, et al. Room temperature photoluminescence of mixed titanium-manganese oxides. J Lumin 2017;187:521–7, http://dx.doi.org/10.1016/j.jlumin.2017.03.015.
[18] Shahnas Beegam M, Narendranath SB, Periyat P. Tuning of selective solar photocatalysis by Mn^{2+} decorated nanocrystalline mesoporous TiO_2. Sol Energy 2017;158:774–81, http://dx.doi.org/10.1016/j.solener.2017.10.046.
[19] Mahmood MA, Baruah S, Dutta J. Enhanced visible light photocatalysis by manganese doping or rapid crystallization with ZnO nanoparticles. Mater Chem Phys 2011;130:531–5, http://dx.doi.org/10.1016/j.matchemphys.2011.07.018.
[20] Villars PKC. Pearson's crystal data crystal structure database for inorganic compounds; 2009.
[21] Mendelson MI. Average grain size in polycrystalline ceramics. J Am Ceram Soc 1969;52:443–6, http://dx.doi.org/10.1111/j.1151-2916.1969.tb11975.x.
[22] Hadžić B, Romčević N, Romčević M, Kuryliszyn-Kudelska I, Dobrowolski W, Narkiewicz U, et al. Raman study of surface optical phonons in hydrothermally obtained ZnO(Mn) nanoparticles. Opt Mater (Amst) 2016;58:317–22, http://dx.doi.org/10.1016/j.optmat.2016.03.033.
[23] Shon HK, Vigneswaran S, Ngo HH, Kim JH. Chemical coupling of photocatalysis with flocculation and adsorption in the removal of organic matter. Water Res 2005;39:2549–58, http://dx.doi.org/10.1016/j.watres.2005.04.066.
[24] Nádherný L, Maryško M, Sedmidubský D, Martin C. Structural and magnetic properties of $Zn_xMn_{3-x}O_4$ spinels. J Magn Magn Mater 2016;413:89–96, http://dx.doi.org/10.1016/j.jmmm.2016.04.029.
[25] Samanta K, Dussan S, Katiyar RS, Bhattacharya P. Structural and optical properties of nanocrystalline $Zn_{1-x}Mn_xO$. Appl Phys Lett 2007;90:261903, http://dx.doi.org/10.1063/1.2751593.
[26] Julien C, Massot M, Poinsignon C. Lattice vibrations of manganese oxides. Spectrochim Acta Part A Mol Biomol Spectrosc 2004;60:689–700, http://dx.doi.org/10.1016/S1386-1425(03)00279-8.
[27] Hadžić B, Romčević N, Romčević M, Kuryliszyn-Kudelska I, Dobrowolski W, Trajić J, et al. Surface optical phonons in ZnO(Co) nanoparticles: Raman study. J Alloys Compd 2012;540:49–56, http://dx.doi.org/10.1016/j.jallcom.2012.06.076.
[28] Venger EF, Melnichuk AV, Melnichuk LY, Pasechnik YA. Anisotropy of the ZnO single crystal reflectivity in the region of residual rays. Phys Status Solidi 1995;188:823–31, http://dx.doi.org/10.1002/pssb.2221880226.
[29] Ashkenov N, Mbenkum BN, Bundesmann C, Riede V, Lorenz M, Spemann D, et al. Infrared dielectric functions and phonon modes of high-quality ZnO films. J Appl Phys 2003;93:126–33, http://dx.doi.org/10.1063/1.1526935.
[30] Das J, Pradhan SK, Sahu DR, Mishra DK, Sarangi SN, Nayak BB, et al. Micro-Raman and XPS studies of pure ZnO ceramics. Phys B Condens Matter 2010;405:2492–7, http://dx.doi.org/10.1016/j.physb.2010.03.020.
[31] Nobbs JH. Kubelka–Munk theory and the prediction of reflectance. Rev Prog Color Relat Top 2008;15:66–75, http://dx.doi.org/10.1111/j.1478-4408.1985.tb03737.x.
[32] Pal M, Pal U, Jiménez JMGY, Pérez-Rodríguez F. Effects of crystallization and dopant concentration on the emission behavior of TiO_2:Eu nanophosphors. Nanoscale Res Lett 2012;7:1, http://dx.doi.org/10.1186/1556-276X-7-1.
[33] Hart JN, Cutini M, Allan NL. Band gap modification of ZnO and ZnS through solid solution formation for applications in photocatalysis. Energy Proc 2014;60:32–6, http://dx.doi.org/10.1016/j.egypro.2014.12.338.
[34] Li F, Liu C, Ma Z, Zhao L. New methods for determining the band gap behavior of ZnO. Opt Mater (Amst) 2012;34:1062–6, http://dx.doi.org/10.1016/j.optmat.2011.12.019.
[35] Özgür Ü, Alivov YI, Liu C, Teke A, Reshchikov MA, Doğan S, et al. A comprehensive review of ZnO materials and devices. J Appl Phys 2005;98:41301, http://dx.doi.org/10.1063/1.1992666.
[36] Morán-Lázaro JP, Guillen-López ES, López-Urias F, Muñoz-Sandoval E, Blanco-Alonso O, Guillén-Bonilla H, et al. Synthesis of $ZnMn_2O_4$ nanoparticles by a microwave-assisted colloidal method and their evaluation as a gas sensor of propane and carbon monoxide. Sensors (Basel) 2018;18, http://dx.doi.org/10.3390/s18030701.
[37] Lakshmi SV, Pauline S. Structural, morpological and optical properties of hetarolite- Znmn 2 and 4 nano particle by hydrothermal method; 2014. p. 8–9.
[38] Zhang P, Li X, Zhao Q, Liu S. Synthesis and optical property of one-dimensional spinel $ZnMn_2O_4$ nanorods. Nanoscale Res Lett 2011;6:323, http://dx.doi.org/10.1186/1556-276X-6-323.
[39] Tuomisto F, Saarinen K, Look DC, Farlow GC. Introduction and recovery of point defects in electron-irradiated ZnO. Phys Rev B 2005;72:85206, http://dx.doi.org/10.1103/PhysRevB.72.085206.
[40] Bergmann K, O'Konski CT. A spectroscopic study of methylene blue monomer, dimer, and complexes with montmorillonite. J Phys Chem 1963;67:2169–77, http://dx.doi.org/10.1021/j100804a048.
[41] Chen L, Li L, Wang T, Zhang L, Xing S, Wang C, et al. A novel strategy to fabricate multifunctional Fe_3O_4@C@TiO_2 yolk–shell structures as magnetically recyclable photocatalysts. Nanoscale 2014;6:6603, http://dx.doi.org/10.1039/c4nr00175c.
[42] Gaya UI. Heterogeneous photocatalysis using inorganic semiconductor solids. Heterog Photocatal Using Inorg Semicond Solids 2014:1–213, http://dx.doi.org/10.1007/978-94-007-7775-0, 9789400777.
[43] Uma R, Ravichandran K, Sriram S, Sakthivel B. Cost-effective fabrication of ZnO/g-C_3N_4 composite thin films for enhanced photocatalytic activity against three different dyes (MB, MG and RhB). Mater Chem Phys 2017;201:147–55, http://dx.doi.org/10.1016/j.matchemphys.2017.08.015.
[44] Xia YJ, Hai LB, Mei SX, Jun Y, An CR. Adsorption of methylene blue and rhodamine B on baker's yeast and photocatalytic regeneration of the biosorbent. Biochem Eng J 2009;45:145–51, http://dx.doi.org/10.1016/j.bej.2009.03.007.